



PHOTONICS Research

Surface acoustic wave photonic filters with a single narrow radio-frequency passband in standard silicon on insulator

MOSHE KATZMAN,^{1,2} MAAYAN PRIEL,^{1,2} INBAR SHAFIR,^{1,2,3} SAAWAN KUMAR BAG,^{1,2}  DVIR MUNK,^{1,2} NAOR INBAR,⁴ MOSHE FELDBERG,² TAL SHARABANI,² LEROY DOKHANIAN,^{1,2} MATAN SLOOK,^{1,2} AND AVI ZADOK^{1,2,*} 

¹Faculty of Engineering, Bar-Ilan University, Ramat-Gan 5290002, Israel

²Institute for Nano-Technology and Advanced Materials, Bar-Ilan University, Ramat-Gan 5290002, Israel

³Soreq NRC, Yavne 81800, Israel

⁴Tower Semiconductors, Migal Ha'Emek 2310502, Israel

*Corresponding author: Avinoam.Zadok@biu.ac.il

Received 1 March 2022; revised 3 May 2022; accepted 3 May 2022; posted 23 May 2022 (Doc. ID 457340); published 30 June 2022

Integrated microwave photonic filters are becoming increasingly important for signal processing within advanced wireless and cellular networks. Filters with narrow transmission passbands mandate long time delays, which are difficult to accommodate within photonic circuits. Long delays may be obtained through slow moving acoustic waves instead. Input radio-frequency information can be converted from one optical carrier to another via surface acoustic waves and filtered in the process. However, the transfer functions of previously reported devices consisted of multiple periodic passbands, and the selection of a single transmission band was not possible. In this work, we demonstrate surface acoustic wave, silicon-photonic filters of microwave frequency with a single transmission passband. The filter response consists of up to 32 tap coefficients, and the transmission bandwidth is only 7 MHz. The results extend the capabilities of integrated microwave photonics in the standard silicon-on-insulator platform. © 2022 Chinese Laser Press

<https://doi.org/10.1364/PRJ.457340>

1. INTRODUCTION

Microwave photonics (MWP) research and development address the generation, distribution, and processing of analog radio-frequency signals using optical means [1–3]. Compared with their electronic counterparts, MWP devices and systems may offer broader bandwidths, longer distribution reaches, comparative immunity to electromagnetic interference, and direct incorporation within fiber communication links [1–3]. Applications within advanced wireless and cellular networks demand the production of MWP systems in larger volumes, smaller size, lower cost, and reduced power consumption [4]. These requirements call for the integration of MWP modules at the chip level [5,6]. Silicon photonics is often the medium of choice for MWP devices, due to the promise of co-integration alongside electronic circuits [7,8].

One of the most important functions of MWP processing is the selection of narrowband channels out of broad optical bandwidths [9,10]. A common filter architecture relies on the splitting of signals among multiple paths, referred to as filter taps, and the weighted summation of their delayed replicas [11]. Narrow spectral passbands require long delays in the

time-domain. Arbitrarily long delays can be realized over fiber paths; however, their coherent addition is prone to environmental drifting [12]. Chip-level delay-and-sum filters provide stable response; however, integrated-photonic waveguides can only support limited delays due to footprint and loss restrictions. MWP filters have been realized in silicon photonic circuits using ring resonators, Mach-Zehnder interferometers, photonic crystals, and cavities [13–15] (for a review, see Ref. [16]). The transmission bandwidths of silicon-photonic MWP filters range between hundreds of MHz and several GHz [16].

Hypersonic acoustic waves are characterized by wavelengths on the optical scale and frequencies that match the rates of information. Acoustic waves, therefore, represent an excellent candidate platform for MWP signal processing. Highly selective, integrated MWP filters have been realized using acoustic waves. Examples include backward stimulated Brillouin scattering in chalcogenide glass waveguides as part of larger silicon-photonic circuits [17,18], forward Brillouin scattering in suspended silicon membrane waveguides [19,20], and electrical actuation in piezoelectric substrates [21]. Reports include

sub-MHz-wide passbands, broad tunability, wide dynamic ranges, and low radio-frequency losses [17–21]. However, these opto-mechanical demonstrations required the supplementing of standard silicon photonics by hybrid material integration or the suspension of structures.

Over the last three years, our group has proposed and demonstrated delay-and-sum MWP filters in standard silicon-on-insulator (SOI) integrated circuits [22–24]. Incoming microwave rate information is converted from the modulation of a first optical carrier to the form of surface acoustic waves (SAWs) through absorption in metallic grating patterns and thermoelastic actuation [25–27]. Information is recovered in the optical domain via photoelastic modulation of a second input optical carrier in a resonator waveguide [22–24]. Slow moving SAWs cross the resonator paths multiple times, imprinting delayed replicas of the input waveform on the output optical carrier. Due to the slow SAWs velocity, delays as long as 175 ns were realized on chip [23,24]. The filter response included up to 12 delayed taps, and the magnitude and radio-frequency phase of each tap could be chosen arbitrarily and independent of those of all others [23]. However, the frequency-domain response of the discrete-time filters consisted of multiple periodic passbands separated by a free spectral range of 65 MHz [23]. In many MWP applications, the selection of a single passband is essential.

In this work, we demonstrate SAW-photonic, discrete-time MWP filters with a single passband of 14 and 7 MHz widths. The number of filter taps is increased to 16 and even 32. The passband frequency can be designed arbitrarily. The experimental results represent a first realization of single-passband, narrow MWP filters in standard SOI, and they further substantiate the SAW-photonic approach for integrated MWP filters with arbitrary transfer functions.

2. PRINCIPLE OF OPERATION

A SAW-photonic, discrete-time integrated MWP filter in SOI is illustrated in Fig. 1. A grating of M metallic stripes with a spatial period Λ is deposited on the SOI layer stack. The grating is illuminated by light from input fiber 1, which is intensity modulated at radio-frequency Ω . Absorption of modulated light in the metals leads to the periodic heating and cooling, which results in thermal expansion and contraction of the grating elements [25–27]. Thermal expansion of the thin metallic stripes takes place on picosecond time scales [25–27]. A strain pattern of spatial period Λ and frequency Ω is, thereby, transferred from the metallic grating to the underlying SOI layer stack and may lead to the generation of SAWs [25–27].

SAW actuation is the most efficient for radio-frequency $\Omega_{\max} = 2\pi v_{\text{ph}}/\Lambda$, where v_{ph} is the phase velocity of a surface acoustic mode of the SOI layer stack [25–27]. For a grating period Λ of 1.4 μm , Ω_{\max} is on the order of $2\pi \times 2.4$ GHz [22]. We denote the normalized frequency response of thermoelastic actuation as $H_G(\Omega)$, with $H_G(\Omega_{\max}) = 1$. The bandwidth $\Delta\Omega_G$ of $H_G(\Omega)$ is on the order of Ω_{\max}/M . Gratings used in this work consist of several tens of periods; hence, $\Delta\Omega_G$ equals tens of MHz. The response $H_G(\Omega)$ of a uniform grating follows a sinc shape and includes spectral sidelobes [28]. The response can be tailored using apodization techniques, such as varying the widths of metallic stripes toward the edges of the grating extent. The magnitude of the generated SAWs is proportional to the intensity modulation of the input optical wave.

A resonator waveguide is patterned in proximity to the metallic grating (see Fig. 1). The resonator layout consists of N straight waveguide sections that run parallel with the grating stripes. Adjacent sections are separated by a fixed lateral offset Δy . The SAW front crosses the parallel waveguide sections with

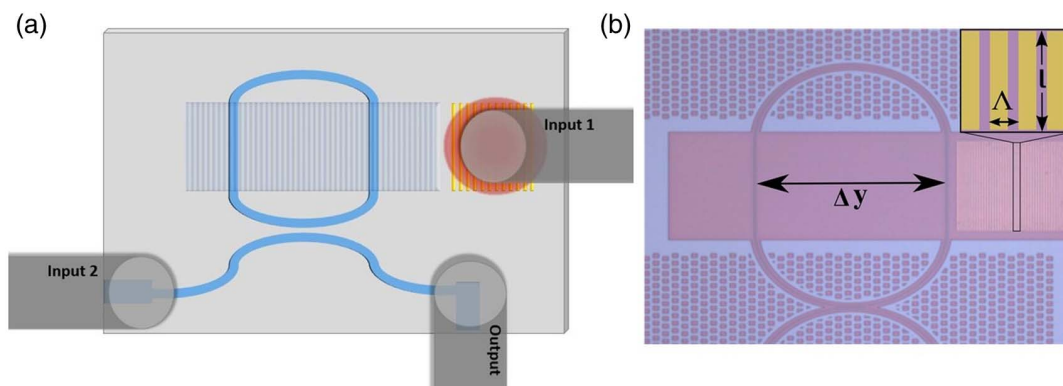


Fig. 1. (a) Schematic illustration of a SAW-photonic, discrete-time microwave filter device in SOI. An optical beam (red) from input fiber 1, modulated by microwave-frequency information, illuminates a grating of metallic stripes (yellow). Thermoelastic expansion and contraction of the grating elements lead to the launch of SAWs, which pass across a resonator waveguide layout. Generation of SAWs is the most effective when the grating period and modulation frequency match those of a surface acoustic mode. Continuous-wave light from input fiber 2 is coupled into the resonator waveguide. The propagating SAWs imprint a replica of the input information onto the guided optical wave in each of N parallel waveguide sections within the resonator layout, via photoelasticity. (The racetrack layout shown in the figure includes $N = 2$ such sections.) Due to the slow acoustic velocities, long delays between replicas are accommodated on-chip. The input microwave frequency information is, thereby, converted from input 1 to the output port, via SAWs. The response of the device is that of a discrete-time, delay-and-sum MWP filter with N taps. (b) Top-view optical microscope image of a fabricated two-tap device (see Section 3). The grating period Λ , the spacing Δy between parallel sections of the resonator waveguide, and the transverse extent l of the grating elements and of the stimulated surface acoustic wavefront are noted on the image.

relative delays of $m\tau_0$ with respect to the section closest to the grating. Here $m = 0, 1, \dots, N-1$, $\tau_0 = \Delta y/v_g$ is a unit delay, and v_g denotes the group velocity of SAWs. The SAWs induce photoelastic perturbations to the refractive index of the resonator waveguide sections.

A second, continuous optical input field is coupled into the resonator waveguide. The exact wavelength of the second input field is locked to a maximal slope of the resonator transfer function [22]. With that alignment, photoelastic modulation along the resonator waveguide is converted to intensity modulation of the guided optical wave at the device output. The normalized time-domain impulse response of the output intensity modulation to SAWs perturbation, in units of s^{-1} , is given by [23]

$$h_R(\tau) = \sum_{m=0}^{N-1} a_m \exp\left(-m \frac{\alpha_{\text{SAW}}}{2} \Delta y\right) \delta(\tau - m\tau_0). \quad (1)$$

In Eq. (1), τ is a time variable, and α_{SAW} [m^{-1}] denotes the propagation loss coefficient of SAWs intensity. At the acoustic frequency of 2.4 GHz, α_{SAW} equals 12 dB \cdot mm $^{-1}$ [23]. The photoelastic modulation response is that of a discrete-time, delay-and-sum filter with N taps [23]. The unitless complex weight a_m of each tap can be designed arbitrarily and independent of those of all others through fine tuning of the width of waveguide section m and its lateral position with respect to $m \cdot \Delta y$ [23]. In this work, we have chosen $a_m = 1$ for all taps.

The frequency-domain response $H_R(\Omega)$ of photoelastic modulation is given by the Fourier transform of $h_R(\tau)$. The periodic response $H_R(\Omega)$ has a maximum value of N . The overall response of the entire SAW-photonic device, from the voltage driving the modulation of the first input optical wave to that of the detected output wave, can be written as

$$H_{\text{Total}}(\Omega) = KH_G(\Omega)H_R(\Omega). \quad (2)$$

The unitless constant K is given by [23]

$$\begin{aligned} K &\approx 2C\bar{P}_1 \exp\left(-\frac{\alpha_{\text{SAW}}}{2}y_0\right) \frac{l}{n_g L} Q(1 - \text{ER})\pi \frac{R\bar{P}_2}{V_\pi} \\ &= 2C\bar{P}_1 \exp\left(-\frac{\alpha_{\text{SAW}}}{2}y_0\right) \frac{l}{\lambda_0} F(1 - \text{ER})\pi \frac{R\bar{P}_2}{V_\pi}. \end{aligned} \quad (3)$$

In Eq. (3), \bar{P}_1 [W] is the average optical power of the first input wave illuminating the metallic grating, and \bar{P}_2 [W] is the average optical power of the second optical wave at the device output. y_0 denotes the separation between the metallic grating and the nearest parallel waveguide section ($m = 0$), L is the resonator waveguide length, and l represents the transverse extent of the propagating SAW front (see Fig. 1). Also, in Eq. (3), V_π [V] is the voltage difference required to switch an electro-optic modulator at the input path of the first optical wave between maximum and minimum transmission, R represents the responsivity of a detector at the device output in $V \cdot W^{-1}$, and $n_g \approx 3.5$ refractive index units (RIU) is the group index of the optical mode in the resonator waveguide. Q , ER, and F denote the quality factor, extinction ratio, and finesse of the resonator, respectively, and λ_0 is the vacuum wavelength of the optical wave guided in the resonator. The intensity modulation of the output wave scales with the spectral sharpness of the resonator transfer function, represented by Q .

The constant C [RIU \cdot W $^{-1}$] in Eq. (3) denotes the ratio between the index perturbation magnitude associated with the generated SAWs and the intensity modulation of the first input wave. C depends on thermoelastic properties of the grating stripes, photoelastic properties of the SOI layers, and the transverse profile of the optical mode in the resonator waveguide. The coefficient C was previously calibrated and found to be on the order of 10^{-6} RIU \cdot W $^{-1}$ [22,23]. End-to-end transmission of optical power through the MWP devices at frequency Ω_{max} may be estimated as N^2K^2 . Due to the comparative inefficiency of thermoelastic stimulation (small value of C), radio-frequency power losses are large: on the order of 70 dB [22,23]. The electrical power transfer function scales with Q^2 . It is degraded by a geometric penalty $(l/L)^2$: the ratio between the extent of the SAW wavefront driven from the grating and the length of the resonator waveguide. Long resonators, therefore, carry a response penalty.

The frequency response $H_{\text{Total}}(\Omega)$ is the product of the envelope function $H_G(\Omega)$, with a peak at Ω_{max} and width $\Delta\Omega_G \approx \Omega_{\text{max}}/M$, and a periodic function $H_R(\Omega)$ with a free spectral range $\text{FSR}_R \approx 1/\tau_0$ and periodic passbands of widths $\Delta\Omega_R \approx 1/(N\tau_0)$. If the separation Δy between adjacent waveguide sections within the readout resonator is short enough, and/or the number of periods M in the metallic gratings is large enough, the free spectral range FSR_R can exceed the envelope bandwidth $\Delta\Omega_G$. In that case, the frequency response of the integrated MWP filter device would consist of a single, narrow passband only. The parallel waveguide sections must be patterned in close separation while maintaining minimal bending radii within the resonator waveguide, so that the quality factor Q is not compromised.

The design of a filter device would begin with choosing the grating period Λ to match a central frequency of choice $\Omega_{\text{max}} = 2\pi\nu_{\text{ph}}/\Lambda$. The separation between waveguide sections Δy would be determined by the required free spectral range $\nu_g/\Delta y$. The number of taps N is selected by the necessary spectral resolution $\nu_g/(N\Delta y)$. Lastly, the tap coefficients $\{a_m\}$ can be chosen using algorithms of digital filter synthesis [12,29]. The exact location and width of each of the N waveguide sections can be adjusted to realize arbitrary complex weights [23].

3. EXPERIMENTAL RESULTS

Devices were fabricated in 8 in. (1 in. = 2.54 cm) SOI wafers with a 220-nm-thick silicon device layer and a 2- μ m-thick buried oxide layer. Optical waveguides were patterned using UV stepper photolithography and inductively coupled plasma reactive ion etching at the Tower Semiconductor commercial silicon foundry. A ridge waveguide cross section was used, with a partial etching depth of 70 nm and core width of 700 nm. Grating couplers were defined at the edges of bus waveguides leading to the resonators. Metallic gratings were subsequently deposited at Bar-Ilan University facilities, using electron-beam lithography, sputtering, and lift-off processes. The grating stripes comprised a 5-nm-thick chromium adhesion layer followed by a 20-nm-thick gold layer. The metallic grating periods Λ were between 1.3 and 1.5 μ m. Alignment markers were used to define the locations of metallic gratings with respect to the resonator waveguides. The separation y_0 between the edges

of the metallic grating and the nearest waveguide section was $4\ \mu\text{m}$.

Figure 2 shows the top-view optical microscope images of 16-tap, 32-tap, and two-tap SAW-photonic devices. The resonator layouts of the 16 (32) tap devices consist of 16 (32) parallel sections with separation Δy of $14\ \mu\text{m}$. The separation corresponds to a unit group delay τ_0 of 3.85 ns. In order to avoid excessive bending losses, the resonator waveguide layouts are folded over so that bending radii remain $50\ \mu\text{m}$ or wider. The lengths L of the resonators are 21.1 mm and 57.1 mm for the 16-tap and 32-tap designs, respectively. The two-tap devices are based on racetrack resonators with $480\ \mu\text{m}$ circumference. The separation Δy between the two straight sections of the racetrack layout is $150\ \mu\text{m}$ (τ_0 of 40 ns). Devices were fabricated in pairs: a 16- or 32-tap device and a two-tap device shared a common metallic grating, located between them [see Fig. 2(e)]. In this manner, photoelastic modulation responses of both devices to the same stimulated SAWs could be compared.

The transfer functions of optical power through the resonator waveguides of devices under test were characterized using an optical vector network analyzer (VNA), with a spectral resolution of $3\ \text{pm}$. Light was coupled between standard single-mode optical fibers and the bus waveguides of the resonator devices using the grating couplers. The coupling losses were 10 dB per interface. Figure 3(a) shows the measured optical power transfer

function of the resonator waveguide in a 32-tap device. The free spectral range of the transfer function is $55\ \text{pm}$. The extinction ratio ER is 15 dB, and the quality factor Q is 125,000.

The experimental setup for the characterization of MWP transfer functions of SAW-photonic devices is illustrated in Fig. 3(b). Light from a first laser diode of $1540\ \text{nm}$ wavelength passed through an electro-optic Mach–Zehnder intensity modulator ($V_\pi = 3.5\ \text{V}$). The modulator was driven by voltage of variable radio-frequency Ω from the output port of an electrical VNA. The modulated waveform was amplified by an erbium-doped fiber amplifier (EDFA) to an average output power \bar{P}_1 of 500 mW and served as input 1 of the device under test. The output fiber of the EDFA was held above the metallic grating of the device under test. The distance between the fiber facet and the device surface was adjusted so that the spot size matched the extent l of the grating.

Continuous-wave light from a second laser diode at $1544\ \text{nm}$ wavelength was coupled into the bus waveguide as the second input of the device under test. The exact wavelength of the source was adjusted to a spectral slope of the optical power transfer function of the device [see Fig. 3(a)], using current and temperature tuning. Due to the sharp slope of the transfer function, the input wavelength was actively locked to the slope using a feedback loop (see Appendix A). The second input wave was modulated along the resonator waveguide by SAWs propagating away from the metallic grating.

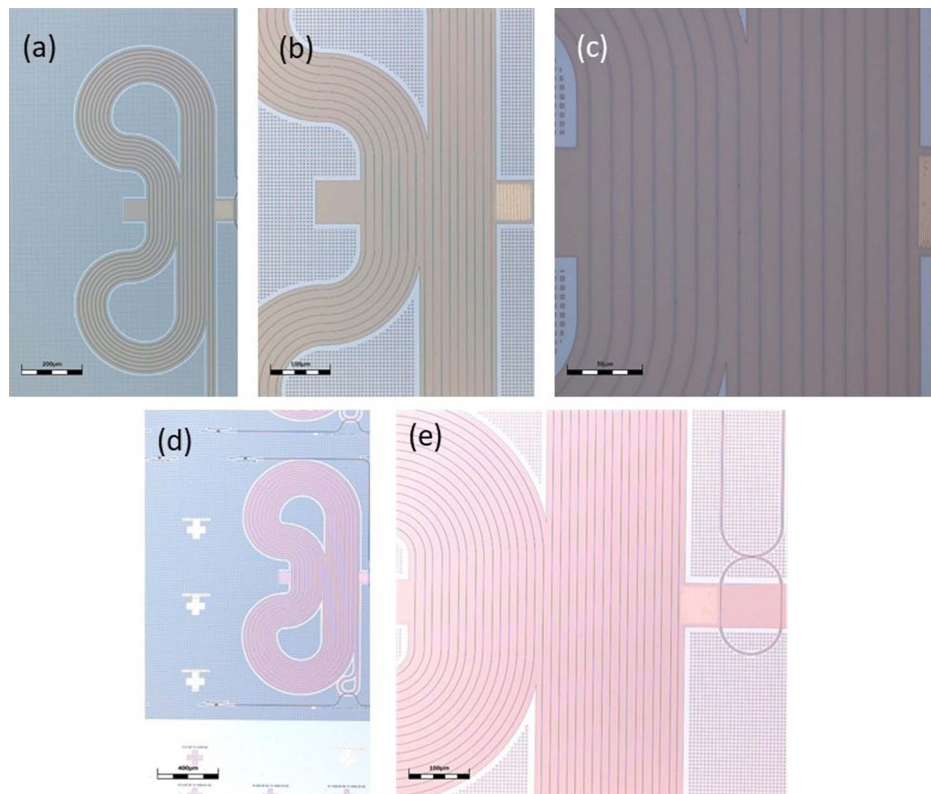


Fig. 2. (a)–(c) Top-view optical microscope images of a 16-tap SAW-photonic MWP filter device. Scale bars correspond to $200\ \mu\text{m}$, $100\ \mu\text{m}$, and $50\ \mu\text{m}$ in the three panels, respectively. A square grating of gold stripes is deposited to the right of a long resonator waveguide. The resonator layout consists of 16 straight sections that run parallel to the grating stripes. (d), (e) Top-view optical microscope images of a 32-tap SAW-photonic MWP filter device. Scale bars correspond to $400\ \mu\text{m}$ and $100\ \mu\text{m}$, respectively. A grating coupler for optical input can be seen at the end of a bus waveguide in the lower left corner of panel (d). A two-tap device to the right of the metallic grating is seen in panel (e).

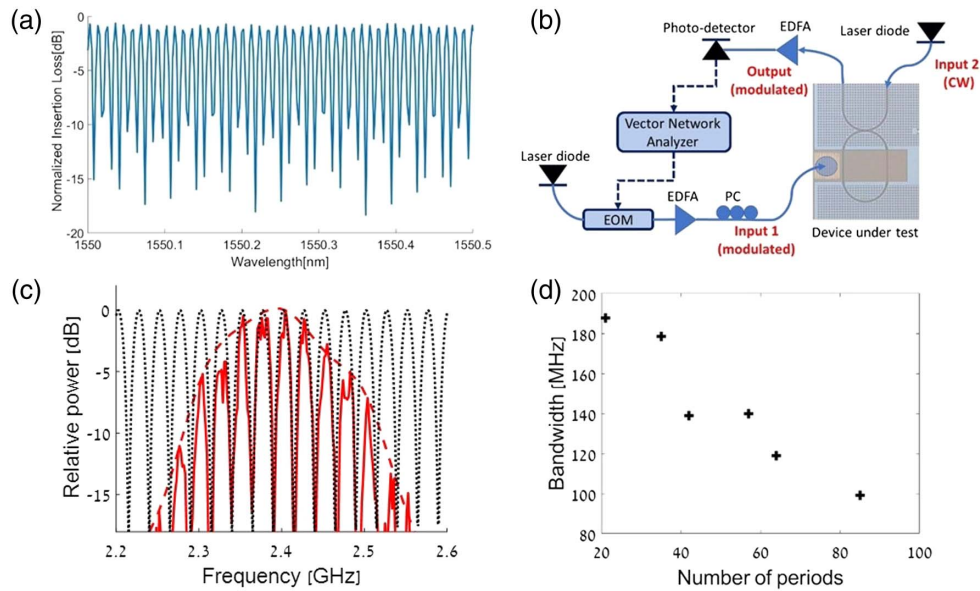


Fig. 3. (a) Measured normalized transfer function of optical power through the resonator waveguide of a 32-tap, SAW-photonic microwave filter device. The free spectral range of the transfer function is 55 pm, and its extinction ratio is 15 dB. (b) Experimental setup used in the measurement of MWP filter device transfer functions. EDFA, erbium-doped fiber amplifier; PC, polarization controller; EOM, electro-optic amplitude modulator; CW, continuous-wave. (c) Solid red, measured normalized transfer function $|H_{\text{Total}}(\Omega)|^2$ of radio-frequency electrical power through a two-tap SAW-photonic filter device. The metallic gratings consisted of $M = 43$ periods, with $\Lambda = 1.4 \mu\text{m}$. Periodic transmission with a free spectral range of 23 MHz is observed. The dotted black trace presents the normalized calculated transfer function $|H_R(\Omega)|^2$ of a two-tap discrete-time filter with the same unit delay of the fabricated device. The periodic response is multiplied with a spectral envelope function $|H_G(\Omega)|^2$ of thermoelastic SAWs stimulation (dashed red). The FWHM $\Delta\Omega_G$ of the envelope bandwidth is 140 MHz. (d) Measured FWHM of thermoelastic SAWs actuation $\Delta\Omega_G$ as a function of the number of periods M in the metallic grating. The width decreases with increasing grating size as anticipated.

The optical waveform at the device output was amplified by a second EDFA to an average power \bar{P}_2 of 5 mW and detected by a photo-receiver of responsivity $R = 27 \text{ V} \cdot \text{W}^{-1}$. The detected voltage was analyzed by the input port of the VNA. The MWP transfer function $|H_{\text{Total}}(\Omega)|^2$ of electrical power through the device was measured by scanning the modulation radio-frequency Ω .

The solid red line in Fig. 3(c) shows the measured $|H_{\text{Total}}(\Omega)|^2$ of a two-tap filter device. The metallic grating of the device consisted of $M = 43$ periods, with $\Lambda = 1.4 \mu\text{m}$. The response is characterized by periodic passbands with a free spectral range FSR_R of 23 MHz (dotted black trace, normalized to a maximum of unity), within a spectral envelope, which represents the response $|H_G(\Omega)|^2$ of thermoelastic SAW stimulation (dashed red trace). The envelope was estimated by sampling the measured response of the two-tap device at the transmission peaks and applying a spectral moving average window. The estimated envelope is asymmetric due to measurement noise and possible acoustic reflections within the grating region. The full width at half-maximum (FWHM) $\Delta\Omega_G$ of $|H_G(\Omega)|^2$ is 140 MHz. The envelope functions $|H_G(\Omega)|^2$ were measured in the same manner for two-tap devices with grating periods of $1.32 \mu\text{m}$ and $1.49 \mu\text{m}$. Figure 3(d) shows the measured $\Delta\Omega_G$ as a function of the number of grating periods M of several two-tap devices ($\Lambda = 1.4 \mu\text{m}$). The bandwidth of thermoelastic stimulation decreases with a larger number of periods as anticipated.

Figure 4(a) shows measured transfer functions of two 16-tap devices with different grating periods Λ . The solid red trace shows the measured $|H_{\text{Total}}(\Omega)|^2$ of a device with $\Lambda = 1.32 \mu\text{m}$, and $M = 43$ periods in the metallic grating. The SAW thermoelastic actuation response $|H_G(\Omega)|^2$ was measured using an adjacent two-tap device through the same metallic grating [dashed red; see Figs. 2(e) and 3(c)]. The peak frequency Ω_{max} of $|H_G(\Omega)|^2$ for the chosen Λ matches one peak of the normalized periodic response $|H_R(\Omega)|^2$ of a 16-tap discrete-time filter with the given τ_0 (dashed black). The free spectral range of $|H_R(\Omega)|^2$ is wider than the bandwidth of $|H_G(\Omega)|^2$. The transfer function $|H_{\text{Total}}(\Omega)|^2$, therefore, consists of a single passband at 2.56 GHz. The FWHM of the passband is 14 MHz, and out-of-band components are rejected by at least 15 dB.

The solid blue trace of Fig. 4(a) presents the measured $|H_{\text{Total}}(\Omega)|^2$ of a second 16-tap device, with $\Lambda = 1.49 \mu\text{m}$ and the same number of periods M . For that grating period, Ω_{max} of the thermoelastic actuation response $|H_G(\Omega)|^2$ (dashed blue) is aligned with an adjacent peak of the periodic term $|H_R(\Omega)|^2$ (dashed black). A single passband is obtained at 2.3 GHz, with FWHM of 14 MHz. Out-of-band transmission is suppressed by at least 12 dB. The red trace in Fig. 4(b) presents the measured $|H_{\text{Total}}(\Omega)|^2$ of a 32-tap device ($M = 43$, $\Lambda = 1.32 \mu\text{m}$). A single passband at 2.56 GHz is observed again. This time, the FWHM of the frequency response is reduced to 7 MHz only, due to the larger number

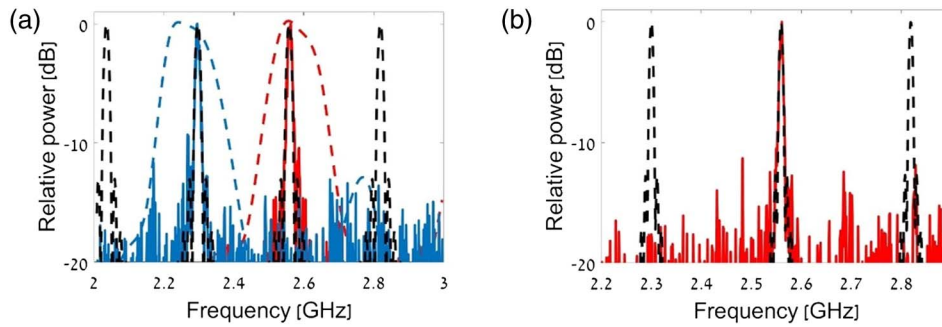


Fig. 4. (a) Solid red, measured normalized transfer function $|H_{\text{Total}}(\Omega)|^2$ of radio-frequency electrical power through a 16-tap SAW-photonic filter device. The period Λ of the metallic grating elements was $1.32 \mu\text{m}$. A single passband at 2.56 GHz frequency with an FWHM of 14 MHz is observed. The transmission of out-of-band components is suppressed by at least 15 dB. The dashed black trace presents the normalized calculated transfer function $|H_R(\Omega)|^2$ of a 16-tap discrete-time filter with the same unit delay of the fabricated device. Additional passbands of the periodic transfer function fall outside the bandwidth of the normalized thermoelastic actuation response $|H_G(\Omega)|^2$ of the chosen grating period [dashed red, measured using an adjacent two-tap device, similar to Fig. 3(c)]. Solid blue, measured $|H_{\text{Total}}(\Omega)|^2$ of a second 16-tap SAW-photonic filter device, with $\Lambda = 1.49 \mu\text{m}$. The frequency response of thermoelastic actuation $|H_G(\Omega)|^2$ for that choice of Λ is offset to lower frequency (dashed blue, measured using an adjacent two-tap device). The single passband is now obtained at 2.3 GHz. The transmission frequency matches a different peak of $|H_R(\Omega)|^2$ (dashed black). (b) Solid red, measured $|H_{\text{Total}}(\Omega)|^2$ of a 32-tap SAW-photonic filter device, $\Lambda = 1.32 \mu\text{m}$. The central transmission frequency is 2.56 GHz. The FWHM of the passband is 7 MHz, and out-of-band components are suppressed by at least 12 dB. Dashed black, calculated $|H_R(\Omega)|^2$ of a 32-tap discrete-time filter with the same unit delay.

of filter taps. Out-of-band transmission is again suppressed by at least 12 dB.

The radio-frequency power losses through the devices are large: 95 dB and 100 dB for the 16-tap and 32-tap filters, respectively. Large losses are due to the relative inefficiency of thermoelastic actuation [22,23] and the long lengths L of the resonator devices [see Eq. (3)]. The ratios between the radio-frequency output power at Ω_{max} and the noise power within 1 Hz bandwidth were $45 \text{ dB} \cdot \text{Hz}^{-1}$ and $40 \text{ dB} \cdot \text{Hz}^{-1}$ for the 16-tap and 32-tap filters, respectively.

4. SUMMARY AND DISCUSSION

Integrated discrete-time MWP filters with single passbands of 14 and 7 MHz bandwidths were demonstrated in standard SOI photonic circuits. The devices are based on the conversion of radio-frequency modulation information from one optical carrier to another, via SAWs. Due to the slow acoustic velocity, long temporal delays are accumulated over path lengths of few hundreds of micrometers. The current study presents several improvements with respect to our earlier work [23]: the number of taps was increased from a maximum of 12 to 32; the free spectral range of the periodic photoelastic modulation response was extended from 65 to 260 MHz; the probe resonator layout was designed for close spacing between parallel waveguide sections while keeping bending losses at a minimum; and the exact locations of waveguide segments were adjusted to account for optical propagation delays in long resonator sections. Most importantly, these modifications have led to single-passband operation with arbitrary transmission frequency, whereas the response of the previously reported filters consisted of multiple, periodic passbands. Single-passband filters are far more suitable for signal processing applications. The filter bandwidths are comparable with those of Brillouin scattering-based integrated MWP devices [17–20]. The

bandwidths are much narrower than those of previous demonstrations of single-passband MWP filters in SOI [13–16].

The main drawback of the proposed devices remains the large losses of radio-frequency electrical power between input and output, measured between 95 and 100 dB. The losses are due to the inherent comparative inefficiency of thermoelastic actuation and increase further by the long lengths L of the resonators. Only a small fraction of the resonator waveguide length is affected by the traveling SAWs wavefront, whose transverse extent l is much smaller than L [see Eq. (3)]. The present losses, however, are not fundamental, and the output signal power may be increased through several solution paths. These include resonators with higher quality factors (Q values over a million were reported in SOI [30]), optimization of the composition and thickness of the metallic grating stripes and their embedding in the silicon device layer [31], amplification of the optical output and its detection with a proper high-power receiver [19,32], and fabrication of shorter resonators with fully etched waveguides that are less susceptible to bending losses. Bending losses in shorter resonator waveguides may also be reduced using elliptical layout and bowed patterns with position-dependent widths [33,34]. Using the above methods, radio-frequency power losses can be reduced by orders of magnitude. Lastly, the architecture of single-passband, delay-and-sum MWP filters can also be realized in piezoelectric substrates, which provide much stronger actuation of SAWs [29,35–39].

Another drawback of the SAW-photonic devices is that their acoustic frequency of operation Ω_{max} cannot be tuned post-fabrication. This challenge is shared by Brillouin scattering-based filter devices as well. Partial solution is found in the mixing between the information of interest and electrical and/or optical local oscillators, at the input or output ends, as proposed in Ref. [19]. While the acoustic frequency of operation does not change, the extended filter device may be tuned to select

arbitrary input frequencies and map them to an output band of choice [19].

The results of this and previous studies establish SAW-photonics as a potential candidate platform for MWP filters and signal processing. Discrete-time filters with up to 32 coefficients and a single passband have been realized in standard SOI. Furthermore, the complex weight of each filter tap may be chosen arbitrarily and independent of those of all others [23]. In addition to MWP, the devices also serve in the analysis of elastic properties of thin layers and interfaces [24]. Future work will be dedicated to the performance enhancement of the devices, toward achieving lower losses and higher signal-to-noise ratios.

APPENDIX A: ACTIVE LOCKING OF THE INPUT WAVELENGTH TO A SPECTRAL SLOPE OF THE RESONATOR TRANSFER FUNCTION

The conversion of photoelastic phase modulation in the resonator devices into an intensity reading at the output requires that the input wavelength should be aligned with a spectral slope of the optical transfer function. The open-loop adjustment of wavelength to a sharp spectral slope of the resonator response is difficult; hence, active locking was employed instead. A signal at frequency $f_{\text{lock}} = 4$ kHz from an output port of a lock-in amplifier was used to directly modulate the drive current of the laser diode source at the resonator waveguide input. The instantaneous optical frequency of the input wave was, therefore, modulated at f_{lock} . Following detection at the device output, a radio-frequency splitter directed part of the retrieved voltage to the input port of the lock-in amplifier. The amplifier tracked the magnitude of the f_{lock} spectral component. That component is the largest at the maximum slope of the resonator response. The lock-in amplifier signal was used in a feedback circuit to correct the laser frequency and keep it at the maximum slope.

Funding. European Research Council (SAW-SBS (101001069)).

Disclosures. The authors declare no conflicts of interest.

Data Availability. Data underlying the results presented in this paper are not publicly available at this time but may be obtained from the authors upon reasonable request.

REFERENCES

- J. Capmany and D. Novak, "Microwave photonics combines two worlds," *Nat. Photonics* **1**, 319–330 (2007).
- A. Seeds, "Microwave photonics," *IEEE Trans. Microw. Theory Tech.* **50**, 877–887 (2002).
- J. Yao, "Microwave photonics," *J. Lightwave Technol.* **27**, 314–335 (2009).
- R. Waterhouse and D. Novak, "Realizing 5G: microwave photonics for 5G mobile wireless systems," *IEEE Microw. Mag.* **16**, 84–92 (2015).
- D. Marpaung, C. Roeloffzen, R. Heideman, A. Leinse, S. Sales, and J. Capmany, "Integrated microwave photonics," *Laser Photon. Rev.* **7**, 506–538 (2013).
- D. Marpaung, J. Yao, and J. Capmany, "Integrated microwave photonics," *Nat. Photonics* **13**, 80–90 (2019).
- L. Pavesi and D. J. Lockwood, "Silicon photonics III," in *Topics in Applied Physics* (Springer, 2016), Vol. **119**, pp. 1–50.
- K. Giewont, K. Nummy, F. A. Anderson, J. Ayala, T. Barwicz, Y. Bian, K. K. Dezfulian, D. M. Gill, T. Houghton, S. Hu, B. Peng, M. Rakowski, S. Rauch, J. C. Rosenberg, A. Sahin, I. Sobert, and A. Stricker, "300-mm monolithic silicon photonics foundry technology," *IEEE J. Sel. Top. Quantum Electron.* **25**, 8200611 (2019).
- J. Capmany, B. Ortega, and D. Pastor, "A tutorial on microwave photonic filters," *J. Lightwave Technol.* **24**, 201–229 (2006).
- R. Minasian, E. H. W. Chan, and X. Yi, "Microwave photonic signal processing," *Opt. Express* **21**, 22918–22936 (2013).
- J. Capmany, B. Ortega, D. Pastor, and S. Sales, "Discrete-time optical processing of microwave signals," *J. Lightwave Technol.* **23**, 702–723 (2005).
- K. P. Jackson, S. A. Newton, B. Moslehi, M. Tur, C. C. Cutler, J. W. Goodman, and H. J. Shaw, "Optical fiber delay-line signal processing," *IEEE Trans. Microw. Theory Tech.* **33**, 193–210 (1985).
- N. Ehteshami, W. Zhang, and J. Yao, "Optically tunable single passband microwave photonic filter based on phase-modulation to intensity-modulation conversion in a silicon-on-insulator microring resonator," in *International Topical Meeting on Microwave Photonics (MWP)* (IEEE, 2015), pp. 1–4.
- S. Song, S. X. Chew, X. Yi, L. Nguyen, and R. A. Minasian, "Tunable single-passband microwave photonic filter based on integrated optical double notch filter," *J. Lightwave Technol.* **36**, 4557–4564 (2018).
- H. Qiu, F. Zhou, J. Qie, Y. Yao, X. Hu, Y. Zhang, X. Xiao, Y. Yu, J. Dong, and X. Zhang, "A continuously tunable sub-gigahertz microwave photonic bandpass filter based on an ultra-high-Q silicon microring resonator," *J. Lightwave Technol.* **36**, 4312–4318 (2018).
- R. Maram, S. Kaushal, J. Azaña, and L. R. Chen, "Recent trends and advances of silicon-based integrated microwave photonics," *Photonics* **6**, 13 (2019).
- B. J. Eggleton, C. G. Poulton, P. T. Rakich, M. J. Steel, and G. Bahl, "Brillouin integrated photonics," *Nat. Photonics* **13**, 664–677 (2019).
- A. Choudhary, I. Aryanfar, S. Shahnia, B. Morrison, K. Vu, S. Madden, B. Luther-Davies, D. Marpaung, and B. J. Eggleton, "Tailoring of the Brillouin gain for on-chip widely tunable and reconfigurable broadband microwave photonic filters," *Opt. Lett.* **41**, 436–439 (2016).
- S. Gertler, E. A. Kittlaus, N. T. Otterstrom, and P. T. Rakich, "Tunable microwave-photonic filtering with high out-of-band rejection in silicon," *APL Photon.* **5**, 096103 (2020).
- S. Gertler, E. A. Kittlaus, N. T. Otterstrom, P. Kharel, and P. T. Rakich, "Microwave filtering using forward Brillouin scattering in photonic-phononic emit-receive devices," *J. Lightwave Technol.* **38**, 5248–5261 (2020).
- Z. Yu and X. Sun, "Acousto-optic modulation of photonic bound state in the continuum," *Light Sci. Appl.* **9**, 1 (2020).
- D. Munk, M. Katzman, M. Hen, M. Priel, M. Feldberg, T. Sharabani, S. Levy, A. Bergman, and A. Zadok, "Surface acoustic wave photonic devices in silicon on insulator," *Nat. Commun.* **10**, 4214 (2019).
- M. Katzman, D. Munk, M. Priel, E. Grunwald, M. Hen, N. Inbar, M. Feldberg, T. Sharabani, R. Zektzer, G. Bashan, M. Vofsi, U. Levy, and A. Zadok, "Surface acoustic microwave photonic filters in standard silicon-on-insulator," *Optica* **8**, 697–707 (2021).
- M. Hen, L. Dokhanian, E. Grunwald, M. Slook, M. Katzman, M. Priel, O. Girshevitz, and A. Zadok, "Analysis of thin layers using surface acoustic wave-photonic devices in silicon-on-insulator," *Opt. Express* **30**, 6949–6959 (2022).
- C. Giannetti, B. Revaz, F. Banfi, M. Montagnese, G. Ferrini, F. Cilento, S. Maccalli, P. Vavassori, G. Oliviero, E. Bontempi, L. E. Depero, V. Metlushko, and F. Parmigiani, "Thermomechanical behavior of surface acoustic waves in ordered arrays of nanodisks studied by near-infrared pump-probe diffraction experiments," *Phys. Rev. B* **76**, 125413 (2007).
- D. Nardi, M. Travagliati, M. E. Siemens, Q. Li, M. M. Murnane, H. C. Kapteyn, G. Ferrini, F. Parmigiani, and F. Banfi, "Probing thermomechanics at the nanoscale: impulsively excited pseudosurface acoustic waves in hypersonic phononic crystals," *Nano Lett.* **11**, 4126–4133 (2011).
- M. Schubert, M. Grossman, O. Ristow, M. Hettich, A. Bruchhausen, E. S. C. Barretto, E. Scheer, V. Gusev, and T. Dekorsy, "Spatial-temporally resolved high-frequency surface acoustic waves on silicon

- investigated by femtosecond spectroscopy," *Appl. Phys. Lett.* **101**, 013108 (2012).
28. T. Erdogan, "Fiber grating spectra," *J. Lightwave Technol.* **15**, 1277–1294 (1997).
 29. C. K. Madsen and J. H. Zhao, *Optical Filter Design and Analysis* (Wiley, 1999).
 30. A. Naiman, B. Desiatov, L. Stern, N. Mazurski, J. Shappir, and U. Levy, "Ultrahigh-Q silicon resonators in a planarized local oxidation of silicon platform," *Opt. Lett.* **40**, 1892–1895 (2015).
 31. M. M. de Lima, W. Seidel, H. Kostial, and P. V. Santos, "Embedded interdigital transducers of high-frequency surface acoustic waves on GaAs," *J. Appl. Phys.* **96**, 3494–3500 (2004).
 32. Y. Liu, A. Choudhary, D. Marpaung, and B. J. Eggleton, "Integrated microwave photonic filters," *Adv. Opt. Photon.* **12**, 485–555 (2020).
 33. L. Zhang, L. Jie, M. Zhang, Y. Wang, Y. Xie, Y. Shi, and D. Dai, "Ultrahigh-Q silicon racetrack resonators," *Photon. Res.* **8**, 684–689 (2020).
 34. R. Li, L. Zhou, J. Xie, A. Xie, and J. Chen, "Optimization of adiabatic microring resonators with few-mode and high-Q resonances," *Appl. Opt.* **54**, 10207–10212 (2015).
 35. M. M. de Lima, F. Alsina, W. Seidel, and P. V. Santos, "Focusing of surface acoustic-wave fields on (100) GaAs surfaces," *J. Appl. Phys.* **94**, 7848–7855 (2003).
 36. M. M. de Lima, M. Beck, Y. Hey, and P. V. Santos, "Compact Mach-Zehnder acousto-optic modulator," *Appl. Phys. Lett.* **89**, 121104 (2006).
 37. H. Li, S. A. Tadesse, Q. Liu, and M. Li, "Nanophotonic cavity optomechanics with propagating acoustic waves at frequencies up to 12 GHz," *Optica* **2**, 826–831 (2015).
 38. D. B. Sohn, S. Kim, and G. Bahl, "Time-reversal symmetry breaking with acoustic pumping of nanophotonic circuits," *Nat. Photonics* **12**, 91–97 (2018).
 39. L. Shao, M. Yu, S. Maity, N. Sinclair, L. Zheng, C. Chia, A. Shams-Ansari, C. Wang, M. Zhang, K. Lai, and M. Lončar, "Microwave-to-optical conversion using lithium niobate thin-film acoustic resonators," *Optica* **6**, 1498–1505 (2019).